

Investigation of an Industrially Scalable Production of Sulfur-Polyacrylonitrile Based Cathodes

Robin Moschner,^{*[a]} Heather Cavers,^[a] Peter Michalowski,^[a] and Arno Kwade^[a]

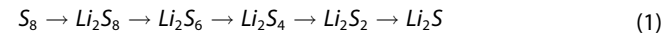
Sulfur-polyacrylonitrile (SPAN) is a sulfur-based active material for next-generation lithium-sulfur battery cathodes. Due to the covalent bonding between sulfur chains and the polymeric backbone, the shuttle effect degrading classical sulfur-based cathodes can be suppressed while also achieving a high active material content in the cathode. In this paper, we investigate the processability of an industrially scalable SPAN active material with 38 wt.-% of sulfur in a water-based and scalable process route. The potential of the SPAN material for industrial adoption and the impact of the process route on the cell

performance are discussed. We show that when processed correctly, the SPAN material delivers exceptional cycling stability and good C-rate performance with ether-based electrolytes. However, the performance of the SPAN cathode is influenced by the mixing characteristic. Using higher mixing intensities during the slurry preparation leads to deterioration of the electrochemical performance. This can be attributed to a decreasing carbon black percolation with increasing tip speed in combination with the kinetic limitation of sulfur cathodes during Li_2S_2 and Li_2S oxidation.

Introduction

Lithium-ion-based batteries are currently used for a wide range of applications, including small-scale consumer electronics like smartphones, laptops, cameras, or cordless screwdrivers, but also medium- to large-scale applications like E-bikes, electric cars, or stationary storage applications. However, especially for larger-scale applications, their current energy density, and specific energy reach their limits, as well as material availability, cost, and eco-friendliness pose a problem.^[1–3] Sulfur itself is an attractive candidate as an alternative cathode active material since its theoretical specific capacity is 1672 mAh g^{-1} , which is much higher in comparison to classical LIB cathode active materials like NCM (up to 210 mAh g^{-1} depending on Ni content) or LFP (up to 170 mAh g^{-1}).^[1,3–6] Also, sulfur is a low-cost and quite abundant material. However, the market introduction of Lithium-sulfur batteries (LSBs) is hindered by multiple sulfur-intrinsic problems. The most prominent hindrance is the so-called polysulfide shuttle. Sulfur, distinct from classical intercalation compounds typically used in LIB cathodes, functions as a conversion-type active material. As such, it undergoes a series of chemical reactions with lithium ions during charge and discharge rather than merely hosting ions within its structure. These reactions form different polysulfide species (Li_2S_x) during multiple reaction steps, as shown in Equation (1). The larger polysulfides (Li_2S_4 to Li_2S_8) are soluble in

the electrolyte, resulting in an increase of the electrolyte viscosity, which decreases the ionic conductivity, as well as the diffusion of polysulfides through the separator into the anode half-cell. This, in turn, leads to unwanted side reactions, which decrease the sulfur cell's electrochemical performance and significantly deteriorate the cycling capacity and C-rate performance.^[3,7–12] Further challenges are the electrically insulating nature of sulfur, which makes a large amount of conductive additive necessary inside the cathode, and the volumetric expansion of sulfur during cell discharge (cathode reduction) of 80%.^[8,10–12]



There are many different approaches in literature to tackle those central obstacles of sulfur as an active material: 1) physical confinement of sulfur in nanoporous conductive materials or even encapsulation,^[3,10,12–16] 2) cathode additives or host structures to chemically confine sulfur reaction products (polysulfides),^[3,10,12,14,16–18] 3) electrolyte engineering/additives^[3,12,19,20] and 4) covalent bonding of sulfur to a host structure/molecule.^[12,19,21–24] All those approaches have their respective advantages and disadvantages.

The covalent bonding of sulfur to a host molecule (e.g., a polymer) prevents the formation of polysulfides in the first place. The bondage of medium-sized sulfur chains (2 to 5 sulfur atoms) leads to a one-phase solid-solid reaction of sulfur and lithium ions to Li_2S_2 or Li_2S .^[24–27] The formation of longer polysulfides is bypassed entirely, eliminating the shuttle effect. This can be observed in the charge and discharge curves of such cells. Typically, sulfur cathodes show two discharge plateaus, the higher one at about 2.3 to 2.4 V created by the reaction of longer and soluble polysulfides (Li_2S_8 , Li_2S_6 , and Li_2S_4) and the lower one at about 2 to 2.1 V is created by the reaction of smaller polysulfides (Li_2S_2 and Li_2S).^[11,12,19]

[a] R. Moschner, H. Cavers, P. Michalowski, A. Kwade
Institute for Particle Technology, Technische Universität Braunschweig,
Volkmaroder Straße 5, 38104 Braunschweig, Germany
E-mail: r.moschner@tu-braunschweig.de

 Supporting information for this article is available on the WWW under
<https://doi.org/10.1002/batt.202400154>

 © 2024 The Authors. Batteries & Supercaps published by Wiley-VCH GmbH.
This is an open access article under the terms of the Creative Commons Attribution License, which permits use, distribution and reproduction in any medium, provided the original work is properly cited.

Cells with covalently bound sulfur show only one charge and discharge plateau with a relatively high voltage gradient. Bypassing longer polysulfides means that these AMs allow for the use of carbonate-based electrolytes and can have highly stable cycling behavior, low impedance values, and high C-rate performance. Additionally, the backbone can reduce and/or buffer the volume expansion and increase the conductivity of the active material. However, the backbone molecule also has to be considered a dead weight in the cell, reducing the specific capacity and, ultimately, the energy density.^[24,27,28] The first material using the covalent bondage of sulfur to a backbone molecule was sulfur-polyacrylonitrile (SPAN), first reported by Wang et al. in 2002.^[29] Since then, many other research groups have carried out investigations on the synthesis process of SPAN,^[28,30,31] its sulfur content,^[23,32] the reaction mechanism,^[24,25,33] or other suitable backbone polymers to increase gravimetric sulfur content.^[22] Additionally, various methods to optimize the sluggish kinetics of SPAN were investigated by multiple research groups over the years, including the use of innovative conductive agents like CNTs or graphene,^[34–39] innovative particle and structural design to reduce diffusion lengths and tortuosity^[40–50] as well as the use of catalytic additives like selenium, tellurium or iodine to decrease the charge transfer resistance and reaction overpotentials.^[40,41,51–56] All these investigations show the importance of good ionic and electric conductivity of SPAN-electrodes on the C-rate and long-term performance.

Since the improvement of the active material kinetics has been a topic of many research papers already, we want to focus on the processability of an industrially scalable SPAN material with 38 wt.-% of sulfur as well as the influence of different slurry mixing parameters on the performance of SPAN cathodes in this paper. This processing aspect has not yet been investigated systematically to the best of our knowledge. Furthermore, production parameters can significantly influence the perform-

ance of batteries, the economics of the production process, and the ecological footprint, which has been extensively demonstrated for classical LIBs by multiple research groups.^[4,57–64] Our results show that increased mixing intensity leads to decreased SPAN cell performance, especially during charging, possibly due to charge-transfer limitations because of lower electrical conductivity and more sluggish reaction kinetics. For this investigation, we used scalable production equipment already established for producing classical LIBs to show the transferability of SPAN electrode production onto already established production lines and possibly Gigafactories. This approach aims to reduce the technological and infrastructural hurdles to a potential market introduction of this new cathode material.

Experimental Section

A purchased SPAN active material by ADEKA CORPORATION containing 38 wt.-% sulfur was used for this investigation. The SPAN cathodes were comprised of 90 wt.-% SPAN AM by ADEKA CORPORATION as well as 5 wt.-% of Super C65 carbon black by TIMCAL Ltd., 3 wt.-% of BM451-B SBR binder (pre-dissolved with 40 wt.-% in deionized water) by ZEON CORPORATION and 2 wt.-% of Texturecel 2000 PA09 CMC binder by DuPont de Nemours, Inc. The electrode production process is loosely based on a lab-scale process developed by ADEKA CORPORATION and was transferred to scalable industry near production equipment like dissolvers and pilot scale coating- and drying devices. The detailed electrode production process is shown in Figure 1.

We started with a 4-step dispersion process in an AE04 dissolver by VMA-GETZMANN GMBH. This relatively complex dispersion process was used to investigate the influence of each sub-step during slurry preparation and is supposed to be simplified in later investigations. First, we prepared a CMC binder solution, which was mixed for 3 hours using a butterfly mixer and then stored for at least 3 days to ensure complete dissolution of the binder in the deionized water. For the slurry preparation, a tooth disc was applied instead. After preparing the binder solution, we added carbon black for pre-

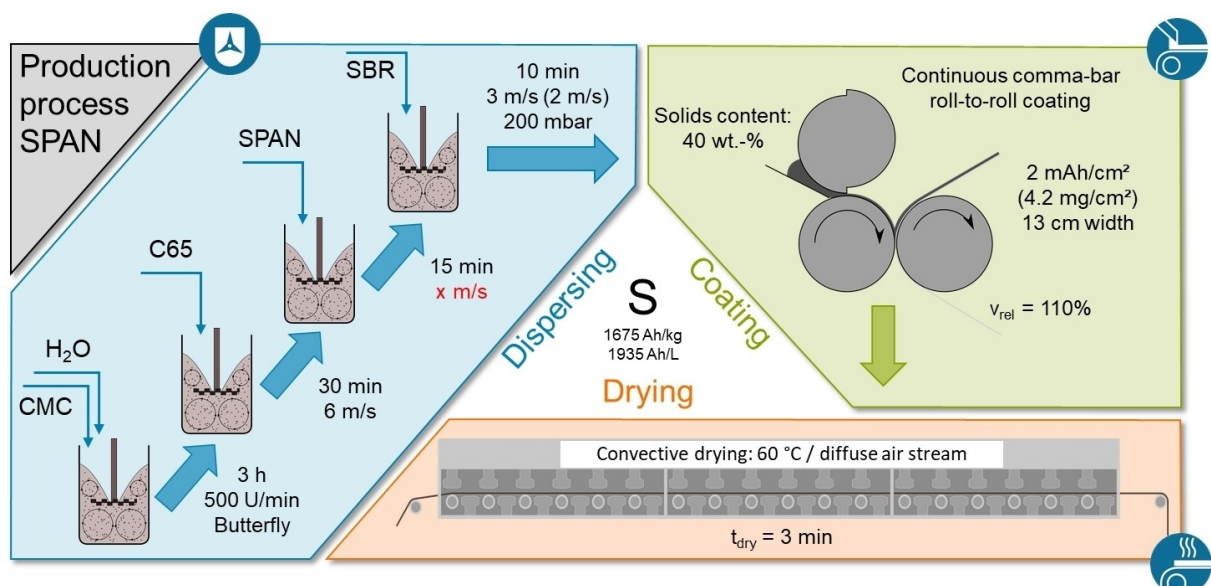


Figure 1. Flow diagram of the electrode production process. The tip speed x shown in red was varied between 2 and 9 $m s^{-1}$ during the investigations.

dispersion at 6 m s^{-1} tip speed for 30 minutes. In the third step, the active material was added and mixed for 15 minutes at different tip speeds ranging from 2 to 9 m s^{-1} to investigate the influence on the active material and electrode properties as well as the cell performance. Even lower mixing tip speeds were not tested due to starting reproducibility issues for such low mixing parameters. In the last step, the shear-sensitive SBR binder was added and mixed for 10 minutes at 3 m s^{-1} tip speed (exception: when the AM was mixed at 2 m s^{-1} , the SBR binder was dispersed with 2 m s^{-1} as well). During this time, the slurry was degassed at 200 mbar absolute pressure. The batch size used was 160 mL, and the target solids content of all slurries was 40 wt.-%.

After the slurry preparation, the batch was transferred to the pilot scale continuous coating and drying device LabCo by KROENERT GmbH & Co KG and coated onto a 15 μm non-coated aluminum foil 1100-L by Speira GmbH using a comma-bar reverse roll coating system as shown in Figure 1. For electrode drying, three convective drying units by Drytec GmbH & Co KG with a length of 2 m each were used. The air direction was set to convective oven mode without direct impingement in all three sections, leading to a gentle drying regime. The used drying temperature was set to 60°C , which led to a necessary drying time of the electrodes of about 3 minutes for the 2 mAh cm^{-2} electrodes. The web speed was set accordingly.

For the LIB cathode and anode reference slurries, NCM622 by BASF and artificial graphite were used as active materials. The LIB cathode slurry comprised 95 wt.-% of NCM622, 1.75 wt.-% Super C65 carbon black and 1 wt.-% of Timrex SFG6 L conductive graphite both by Timcal Ltd. and 2.25 wt.-% of Solef PVdF 5130 by Solvay in NMP with a solids content of 70 wt.-%. The LIB reference anode slurry was comprised of 95 wt.-% of graphite, 1 wt.-% of Super C65 by Timcal Ltd., 3 wt.-% of BM451-B SBR binder by ZEON CORPORATION, and 2 wt.-% of Texturecel 2000 PA09 CMC binder by DuPont de Nemours, Inc. in deionized water. The target solids content was 47.5 wt.-%. Both slurries were processed in the already described dissolver by VMA-GETZMANN GMBH with different mixing procedures. For the NCM cathode slurry, all components were dry-mixed at low intensity before being introduced into the NMP solvent within the dissolver. The slurry was mixed at 9 m s^{-1} for 30 minutes with an absolute degassing pressure of 200 mbar in the last 15 minutes. For the anode the active material, carbon black and CMC binder were dry mixed at low intensity and then introduced into deionized water in the described dissolver. The mixing speed was set to 9 m s^{-1} and kept for 10 minutes. Finally, the SBR binder was introduced, and the mixing speed was reduced to 3 m s^{-1} for 15 minutes at 200 mbar total pressure.

Investigations and measurements were performed along the whole process chain, beginning with the pristine active material and ending with the cells. In- and offline measurements were carried out during the individual process steps to gain insight and derive process-structure-property relationships. An overview of the performed measurements along the production chain is given in Figure 2.

Pristine Active Material

The particle size distribution of the active materials was characterized using the laser diffraction device Partica LA-960 by HORIBA Scientific in dry mode. The device uses a wavelength of 650 nm for particle size measurement in the range of 10 nm to 5 mm. A vibrating feeder and compressed air were used for sample insertion and deagglomeration. The particle size distribution was derived by combining at least seven individual measurements using a diffraction index for the SPAN material of 1.69–0.24i approximated

empirically using the LA-960. The diffraction indices used for NCM622 and graphite were 1.50–0.10i and 1.70–0.05i, respectively.

The pristine SPAN active material was further characterized regarding its specific surface area using an ASAP 2460 BET device by Micromeritics Instrument Corporation via a five-point BET measurement. For each sample, three individual measurements were carried out using about 1.5 g of total sample mass, respectively. Nitrogen was used as the adsorptive and coolant. The samples were prepared by overnight heating at 80°C under vacuum to remove adsorbed water from the material.

Slurries

During the different sub-steps, the slurries were characterized using rheological measurement techniques, which gave insight into the networking and interactions of the components, as well as the coating and shelf life behavior. In parallel, particle size measurements of the whole slurry and the carbon black were carried out for additional information about the carbon black dispersion progress.

The rheological slurry behavior was characterized using a shear rate and an amplitude sweep test with a Kinexus Pro+ by NETZSCH-Gerätebau GmbH. For both measurements, a cone-plate geometry with a cone angle of 4° was used at 20°C . To ensure good contact, a 2-minute long pre-shear phase with a shear rate of 0.01 s^{-1} was implemented for both measurements. The shear rate test included a logarithmic shear rate ramp between 0.01 and 500 s^{-1} . To characterize the slurry's complex shear rate behavior, an amplitude sweep with a constant frequency of 1 Hz was performed. The applied complex shear stress was increased logarithmically from 0.01 to 500 Pa.

The particle size, especially of the carbon black, significantly affects the electrical resistivity of electrodes and the rheology during mixing due to its close interaction with the binder. Therefore, the particle size of the carbon black was measured along the slurry production process also using the Partica LA-960 device by HORIBA Scientific, employing two lasers with wavelengths of 405 nm and 650 nm, respectively. The measurement procedure is derived and simplified from the method described by Dreger et al.^[65] The SPAN slurry samples were prepared by mixing 0.5 g of slurry with 12 g of deionized water, followed by centrifugation for 5 min at 500 rpm, if needed, with an outer centrifuge diameter of 248 mm (equivalent to 34.7 g). The centrifugation was performed to separate the smaller porous carbon black particles and the more compact and larger SPAN particles. The carbon black diffraction index used was 1.76–0.262i. Each measurement was carried out as two triple measurements.

Electrodes

The produced electrodes were characterized regarding their structural and electrical properties to gain detailed insight into the influences of the process variations on the electrode structure and to link these intermediary product properties with the electrochemical properties of the cells.

The structural characterization was done using BET and mercury intrusion porosimetry measurements. The BET measurements were carried out as described above for the pristine active material. However, as sample preparation, 100 cm^2 of electrodes were cut into small pieces. Each BET measurement was carried out thrice. The pore size distribution of the different electrodes was characterized by mercury intrusion porosimetry using a PoreMaster GT 60 by Anton Paar GmbH, as described by Froboese et al.^[66] As sample preparation, an electrode area of 40 cm^2 was cut into small pieces

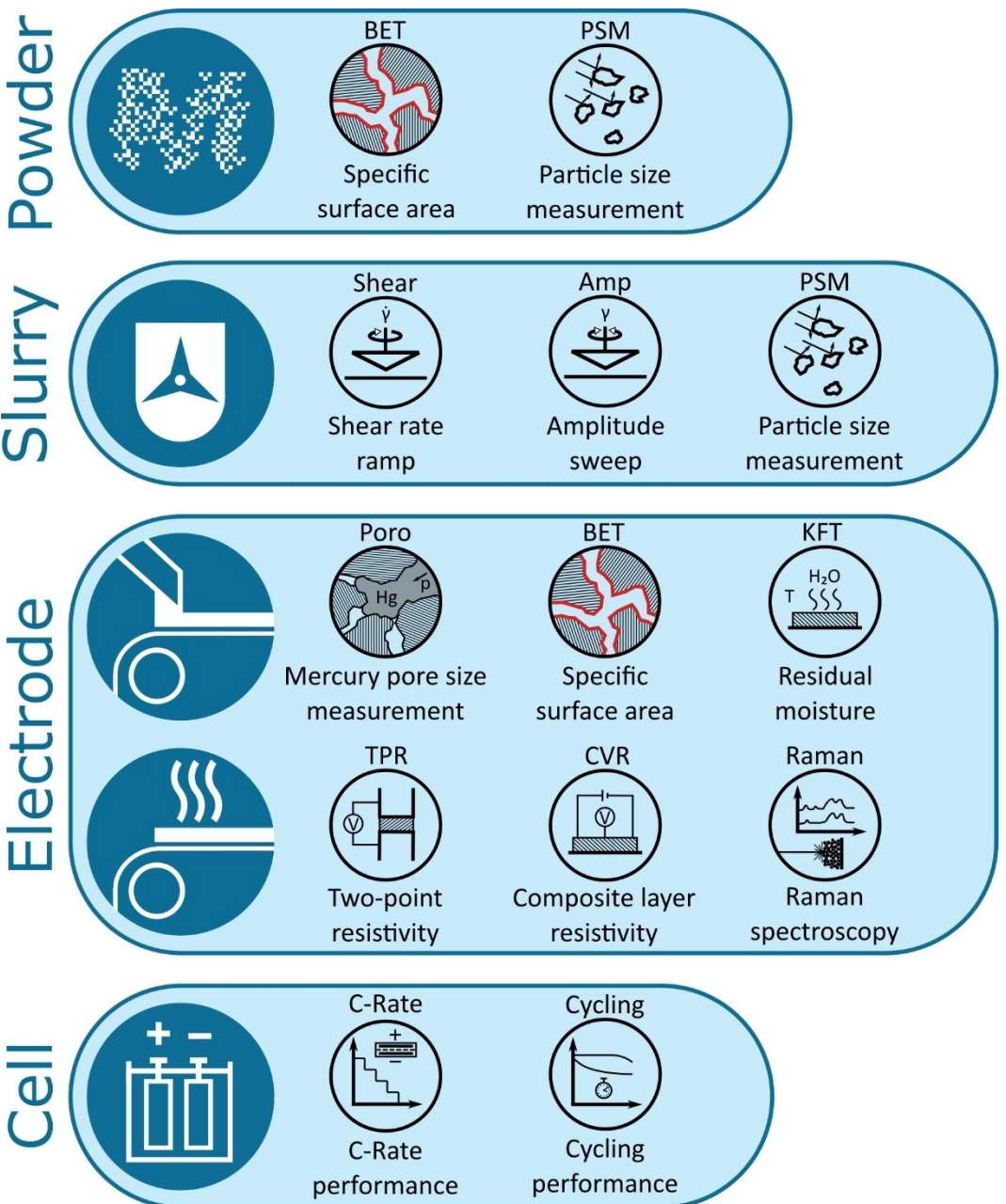


Figure 2. Overview of the used measurement techniques for the pristine material as well as the intermediate and final products covered in this study.

and inserted into the measurement device. The pressure range was set from 10 to 30.000 PSI (measuring pore sizes of 7 nm to 21 μm). Each electrode was measured twice.

As one crucial factor regarding the performance of cells, the electrical conductivity of the electrodes was characterized by two different methods. One is a two-point measurement described in more detail by Westphal et al.^[67] A 1.13 cm^2 sample is pressed between two parallel areal contact points with 0.35 MPa by the Z2020 (ZwickRoell GmbH & Co. KG) to ensure good electrical contact. While applying pressure, a current of 50 mA is used to measure the top-to-bottom resistivity of the sample via the voltage. Ten individual measurements were done for each electrode type. In parallel, composite resistivity and contact resistance measurements of these electrodes were carried out using an Electrode Resistance Measurement System RM2610 by HIOKI E.E. CORPORATION. This

system applies a constant current on the sample's surface and measures the potential distribution at multiple points. From this data, both values can be derived separately. 30 measurements were done for each electrode to receive the values shown in this research.

The residual moisture of the electrodes was measured by coulometric Karl Fischer Titration (KFT) using an Aqua 40.00 with a headspace module by ECH Elektrochemie Halle GmbH. The samples were prepared by stamping three 12 mm diameter samples for each electrode. The samples were sealed in gas-tight sample glasses and inserted into the machine. The moisture amount was measured by titration at 120 °C for 15 min. The procedure of the KFT measurement is described in more detail by Huttner et al.^[68]

The Raman measurements on pristine electrodes were done using a WITec alpha300 R Raman microscope by Oxford Instruments plc with a 532 nm laser to investigate chemical changes of the active material. The measurements were carried out with a laser power of 2 mW and a 50x optical magnification. Each result was calculated by averaging ten individual measurements at different positions. For every individual measurement, 30 accumulations with integration times of 0.5 s apiece were recorded. The dry electrodes were characterized as produced.

Cell tests were carried out on a coin cell level using CR2032 format. The cells were assembled in an argon glovebox with oxygen and water content both below 3 ppm. A 14 mm diameter cathode was set against a 15 mm diameter rolled lithium anode with 500 µm thickness by RodaChem BV and separated by a Celgard 2500 by CELGARD, LLC with a diameter of 16 mm. The separator was wetted from both sides with a total of 50 µL Diglyme-based electrolyte containing 0.325 M LiTFSI and 0.675 M LiNO₃ as conductive salts purchased from E-Lyte Innovations GmbH. Since this study focuses on cathode development, no extensive electrolyte screening was done. An ether-based electrolyte was chosen instead of a carbonate-based one due to its higher compatibility with the lithium metal anode. Preliminary tests have shown that the diglyme-based electrolyte has better long-term stability than a DOL:DME-based electrolyte, which is why it was used for the investigations described here. The cell stack was sandwiched with spacers until reaching a total stack height of around 2.08 mm. The cell was crimped after adding a wave spring.

The cells were cycled between 1 and 3 V vs. Li⁺/Li at 25 °C. After 24 h of rest to ensure good wetting, 5 initial cycles were run at 1/10 C CC charge and discharge to set up the cell. Subsequently, a discharge C-rate test was carried out using 1/10 C, 1/3 C, 1 C, and 2 C, followed by a charge C-rate test with the same C-rates. Finally, all cells were cycled at 1/3 C CC symmetric for 100 cycles. During specific cycles in the procedure, the internal cell resistance was measured by applying 1 C charge and discharge pulses at 50% SOC based on Ryll et al.^[69] The cycling procedure is described in more detail in Table S1 and Table S2 in the supporting information. Four cells were built for each electrode, and at least three were evaluated. The electrochemical tests were conducted using a Cell test system (CTS) by BaSyTec GmbH and a climate chamber by BINDER GmbH.

Results

The processing behavior and processing stability of a material during dispersion define the complexity of this step, as well as the further processability during coating and drying, due to the formation of the particle network, the sedimentation stability, and the behavior in the coating device. Essential parameters for the processability of the material are the particle size distribution and the rheological properties. Some key differences can be found when comparing the pristine SPAN material to classical LIB materials, such as synthetic graphite and NCM622. Knowledge of these differences is essential for adjusting the process parameters when shifting from classical LIB-electrode production to SPAN-electrode production.

Comparing the particle size distributions of these three pristine active material powders in Figure 3(a), it can be seen that NCM622 particles are in a similar particle size range as the SPAN material used here but show a much more narrow distribution. In contrast, graphite particles are usually larger.

The broad particle size distribution of the SPAN used here, ranging down to relatively small particles combined with a microstructured and irregular particle structure, leads to a high specific surface area of about 12.7 m² g⁻¹, which is about 4 times the surface area of the synthetic graphite and about 40 times the surface area of the NCM622. This high surface area directly impacts the achievable solids content in the slurry since a higher surface area leads to less free solvent and, therefore, to more particle-particle interactions, which increases viscosity.^[4] At the same time, the material density of SPAN is lowest for the three materials with about 1.90 g cm⁻³, compared to 2.25 g cm⁻³ for graphite and 4.75 g cm⁻³ for NCM622. This results in a higher volumetric solids content for the same gravimetric solids content, also increasing viscosity. Therefore, the solids content in the SPAN slurry was set to 40 wt.-% or 26.7 vol.-% for all electrodes.

Figure 3(b) shows the shear rate dependent viscosity of SPAN slurries mixed at 3 and 9 ms⁻¹ compared to a synthetic graphite anode and a NCM622 cathode slurry. The SPAN slurry demonstrates a shear thinning behavior comparable to the NCM622 cathode slurry. This behavior is very favorable for industrial production since a high low-shear viscosity corresponds to good sedimentation stability and good edge formation during coating, while a low high-shear viscosity is crucial for a good and homogeneous general coating behavior in the coating device.^[4,70] Since the SPAN cathode uses the same binders as the graphite anode, it is remarkable that the shear rate behavior is much more favorable in comparison. This might be due to the higher additive amount in the SPAN cathode but can also be attributed to the active material itself. The higher specific surface area, the smaller particle size, and probably also the different surface properties lead to better network formation in the slurry, which is observable in the form of the high low-shear viscosity.^[71]

Figure 3(c) shows the complex rheological behavior of these three different slurry types including SPAN slurry mixed at two different tip speeds measured via an amplitude sweep. The depicted phase angle describes the ratio between elastic and plastic slurry behavior: a phase angle of <45° indicates a gel-like slurry behavior, while a phase angle >45° indicates free-flowing viscous slurry behavior.^[72,73] As visible in Figure 3(c), the SPAN and NCM cathodes both show gel-like slurry behavior for lower shear stresses, further improving the sedimentation stability since particles have more restricted movement in gel-like slurries. For higher shear stresses, all slurries have free-flowing viscous slurry behaviors, which is essential for good processability in the subsequent coating step.^[70,72,73]

Combining all the properties described above, the SPAN slurry demonstrated favorable and homogeneous coating results with doctor blade, comma bar, and slot die (Figure S1). This means there are no major obstacles to the general scalability and transferability of this material to industrial scale on already established LIB production equipment from material to electrode. It even benefits from experiences already collected for these electrodes during coating (NCM cathodes – because of similar rheology) and drying (Graphite anodes – because of the same binder-solvent combination). However, this transfer

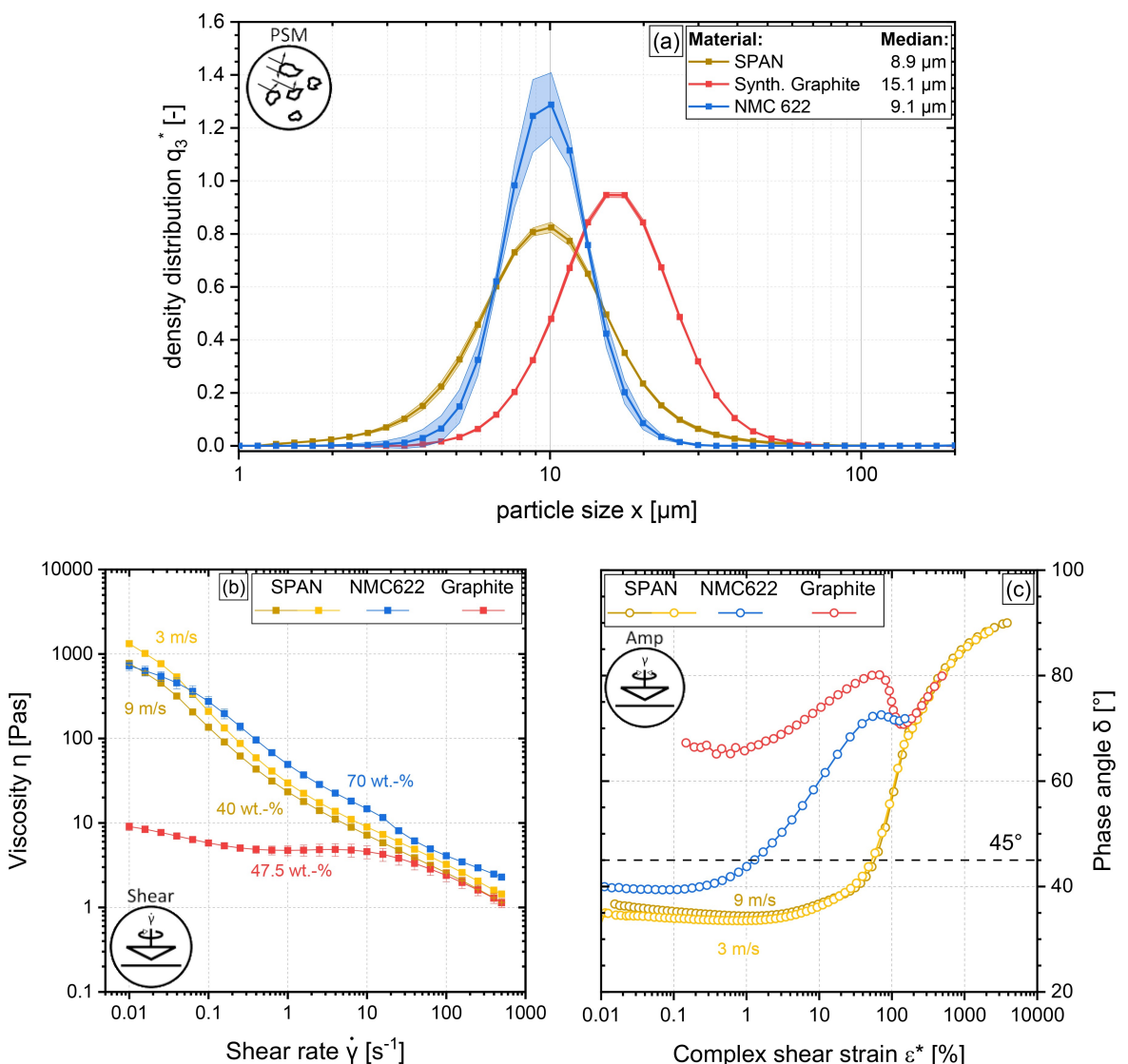


Figure 3. Particle size distribution of the pristine powders of SPAN, NCM622, and synthetic graphite (a); Rheological characteristics of SPAN (dispersed at 3 and 9 m s^{-1}), Graphite and NCM622 based electrode slurries during shear rate tests (b) and amplitude sweep tests at 1 Hz (c).

requires further investigation. In particular, the mechanical process limits of the polymer-based materials have to be investigated to prevent any performance-harming damage. Therefore, different tip speeds were examined following the addition of the active material. Both the intermediary products and the finished electrodes were characterized along the way to quantify the impact of this critical parameter on the electrode structure and properties. Information about the differences in the rheological behavior and the particle size distribution of the different slurries can be found in Figure S2 of the supplementary information. It shows that with increasing tip speed the viscosity of the slurry decreases slightly due to more distinct carbon black deagglomeration while remaining strictly shear-thinning.

The electrodes were subjected to electrochemical evaluations to investigate the impact of different tip speeds on the electrochemical performance. The cycling capacity results are shown in Figure 4(a). It is obvious that for the lower tip speeds

like 2 and 3 m s^{-1} , the cycling performance is very stable, while the coulombic efficiency is at 100%. This good long-term stability is combined with a high C-rate performance of up to 2 C. For 2 m s^{-1} , the capacity retention is above 90% for 2 C discharge and above 80% for 2 C charge, as shown in Figure 4(b). However, this good performance is not characteristic of all processing parameters. At higher tip speeds, the achievable capacity during long-term cycling and the capacity fading worsen. As shown in Figure 4(c), the attainable capacity at the start of the long-term cycling at 0.33 C begins to drop dramatically for tip speeds higher than 4 m s^{-1} , while the capacity fading increases linearly with the applied tip speed during mixing. Interestingly, the coulombic efficiency for all tip speeds remains at 100% during cycling. That, combined with high capacity retention for all cells during the recovery cycles at 0.1 C, indicates a growth in the charge transfer resistance.

Further analyzing the C-rate performance of the different electrodes in Figure 4(b) reveals a slight reduction of the

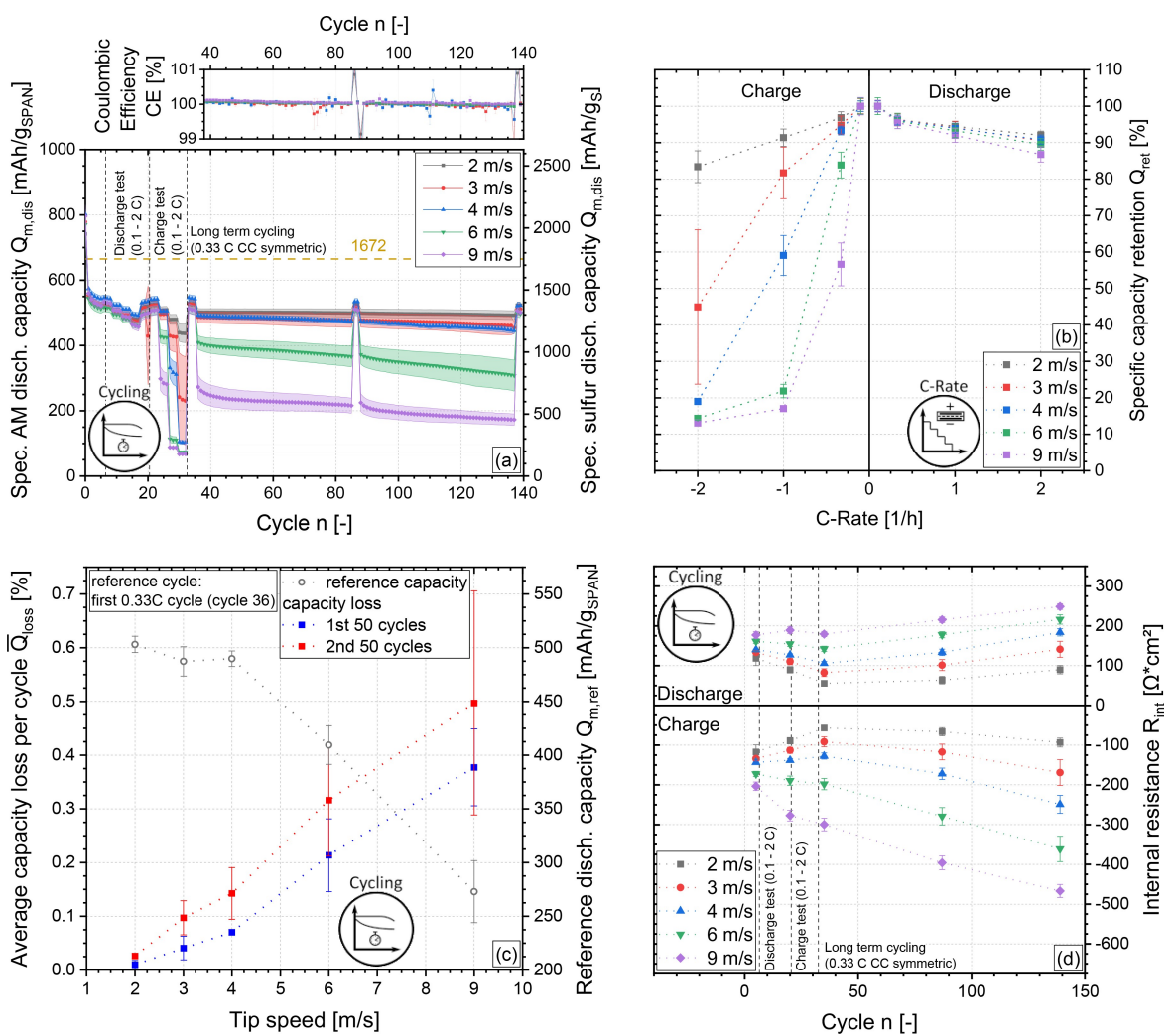


Figure 4. Cycling performance of electrodes mixed with different tip speeds in coin cells (a); Capacity retention based on 0.1 C-rate for charge and discharge (b); Capacity values as well as the capacity fade per cycle during the long-term cycling test (c); Internal resistance development in charge and discharge direction at SOC 50 for different tip speeds (d).

discharge capacities but a much more significant decrease in the charge performance. The achievable capacities for 1 and 2 C decrease first, even for 3 and 4 m s^{-1} . This explains why the reference capacity for long-term cycling is not significantly impacted up to 4 m s^{-1} since it is cycled at 0.33 C, and the 0.33 C capacity is still comparatively good. For 6 m s^{-1} , the capacities at 1 and 2 C decrease even further, and the 0.33 C performance also drops during charging. For 9 m s^{-1} , the capacity decline at 0.33 C becomes even more severe, while the capacities at 1 and 2 C seem to stabilize at around 15% of the 0.1 C capacity. This gradual capacity drop for increasing tip speeds starting at higher C-rates indicates an overpotential growth in the cell. This also explains why the capacity at the start of the long-term cycling for 4 m s^{-1} shown in Figure 4(c) is still relatively high, but the capacity fade per cycle is increasing by roughly 300% compared to 2 m s^{-1} . The charge voltage may be partially shifted out of the chosen voltage range due to the growing overpotentials during cycling, which leads to propagating capacity loss.

To get further insight, internal resistance measurements were done at SOC 50 with a 1 s long charge and discharge pulse of 1 C. The results for the electrodes processed at different tip speeds are shown in Figure 4(d). The tests were carried out after the initial setup cycles, after the discharge C-rate test, after the charge C-rate tests, and after each long-term cycling loop of 50 cycles, respectively. Looking at the electrode processed at 2 m s^{-1} , the internal resistance values are nearly symmetric for charge and discharge. Interestingly, the internal resistances of the 2 m s^{-1} cells decrease at first during the C-rate tests and reach their lowest value of about 55 Ωcm^2 after those tests. During the long-term cycling, the internal resistance increases again to about 65 Ωcm^2 and 90 Ωcm^2 after each 50-cycle loop, respectively. The increase during the second loop is more prominent, which explains the increased fading of the cell capacity per cycle for the second cycling loop, shown in Figure 4(c). This should be due to cell aging, i.e., propagating SEI formation because of dendrite formation on the anode. However, the initial decrease of the internal cell resistance

seems to be based on a different mechanism. Looking into the differential capacity characteristics of the 2 m s^{-1} cells at 0.1 C, as shown in Figure S3(a), there is no major change during the cycling. However, the internal resistance may not impact the 0.1 C voltage characteristic as much since the C-rate is very low. Further investigations with higher C-rates after extended cycling might shed more light on this aspect. At this point, we propose that the initial cycles, including the C-rate tests, significantly influence the SEI formation, which was already shown for LIB cells.^[74,75] This might result in a SEI reformation and restructuring in the earlier cycles, especially since higher C-rates influence the lithium solution and deposition. Furthermore, SPAN is known to improve its kinetics in the first cycles due to lithiation of the PAN backbone, which enhances the conductivity and charge-transfer resistance of the material.^[24,76]

However, this is not the only interesting aspect visible in Figure 4(d). Another aspect is the internal resistance increase with rising tip speeds. This aligns with the results described earlier regarding the C-rate performance and the capacity fade. An elevated internal resistance would lead to increased overpotentials, resulting in capacity loss. However, the increase in internal resistance is not symmetric. For increasing tip speed, the internal charge resistance grows significantly more than the internal discharge resistance. While the internal resistance at the end of the cycling procedure increases from 2 to 9 m s^{-1} by about 175% in the discharge direction, the resistance jumps up by nearly 400% in the charge direction. Furthermore, the v-shape of the resistance profile evolves into a strictly linear growth over the whole cycling procedure for higher tip speeds, indicating that harmful aging-related effects are becoming more significant compared to initial advantageous mechanisms. Again, this is especially distinct in charge direction. These effects align with the cycling and C-rate results shown before. An increased internal resistance especially harms the performance at higher C-rates, while the impact on the low C-rate performance is limited. In addition, a higher internal resistance in the charge direction is the reason for the worse charge C-rate performance compared to the discharge performance.

Although the internal resistance in the discharge direction is also increasing notably, the discharge C-rate performance is not significantly impacted. Further insight is provided by the voltage characteristics in differential capacity plots, shown in Figure 5. Increasing tip speeds shift the charge voltage peak towards higher values, even beyond the used voltage range, leading to massive capacity loss. By comparison to Figure 5(a), it is evident that first, the 2 C charge peak is shifted beyond 3 V for 3 m s^{-1} (b), then followed by the 1 C charge peak for 4 m s^{-1} (c) and the 0.33 C peak for 9 m s^{-1} (e). The shift of the charge voltage plateau can also be seen in the according voltage curves presented in Figure S4 and explains the gradual capacity loss during C-rate tests for increasing tip speeds shown in Figure 4(b). However, the discharge peak is not so much shifted as compressed within the dQ/dU plots, visible in the voltage curves as a flattening of the discharge plateau for higher tip speeds and C-rates.

Looking deeper into the discharge characteristic, the peaks are also slightly shifted towards lower voltage values but are

mainly compressed. This could indicate that during discharge, the Li_2S_2 formation is primarily affected by the C-rate and, therefore, shows larger overpotentials than the Li_2S formation located at the lower voltage end. For increasing tip speed, the 2 C discharge peak of Li_2S_2 is shifted by about 0.3 V to lower voltage values (2 m s^{-1} to 9 m s^{-1}). Simultaneously, the Li_2S discharge peak is only moved by about 0.15 to 0.2 V. Additionally, it can be seen that the voltage jump at the start of the discharge is much more significant for higher tip speeds, even going below the voltage value of the Li_2S_2 discharge peak. The result is a recovery of the voltage after the initial sharp drop. This phenomenon starts showing at 2 C discharge for 4 m s^{-1} , as visible in Figure 5(c), increasing its severity for 6 and 9 m s^{-1} . At 6 m s^{-1} , it also becomes visible for a discharge at 1 C, as depicted in Figure 5(d). These characteristics might be due to a kinetic limitation at the beginning of the discharge step. Li_2S_2 and Li_2S are both solid products. Previous investigations into the mechanistic behavior of reaction product formation during the cycling of SPAN material have indicated that Li_2S_2 and Li_2S form small crystallites within the cathode.^[24] Since Li_2S_2 forms first at higher voltages, it starts the nucleation, which is connected to higher kinetic limitations.^[77,78] After the initial nucleation, Li_2S_2 reacts further to Li_2S , which is a solid-phase transformation without forming new solid structures in the electrode. Therefore, the kinetic limitations, and with them the discharge overpotentials, should be significantly lower for the Li_2S formation than for the Li_2S_2 formation. This would explain why the Li_2S peak is much less impacted by higher C-rates than the Li_2S_2 peak. However, further in-depth mechanistic research must be done to clarify the mechanisms involved here.

It is evident by comparing Figure 5(a) to (e) that the voltage shift of the discharge peak, especially for Li_2S , is much less significant than the shift of the charge peak for increasing C-rates and tip speeds. This correlates well with the internal resistance measurements shown in Figure 4(d) and indicates that either the Li deposition on the Anode or the Li_2S_2 and Li_2S oxidation in the cathode are highly impacted by those factors. Since the anode is initially the same for all the cells shown here, the lithium deposition reaction can be ruled out as the factor correlating with the tip speed. Therefore, the reason for the different performances must be connected to the cathode. Multiple aspects can affect the electrochemical performance and the internal resistance of the cells on the cathode side. The first factor could be mechanical damage to the active material in the wake of higher tip speeds. Smaller or cracked-open particles might lack surface functionalization or integrity to perform well or face more intense side reactions due to a higher surface area.^[76,79–81] The second potential reason might be changes in the reaction mechanism of the active material due to process impact, while the third potential factor could be a decreased ionic conductivity caused, for example, by higher tortuosity or lower porosity.^[82–84] Finally, the fourth factor affecting the electrode performance may be a worse electrical connection of the active material particles due to more intense carbon black deagglomeration.^[67,85,86]

Mechanical damage to the active material, like particle breakage and fracturing, should be visible by changes in the

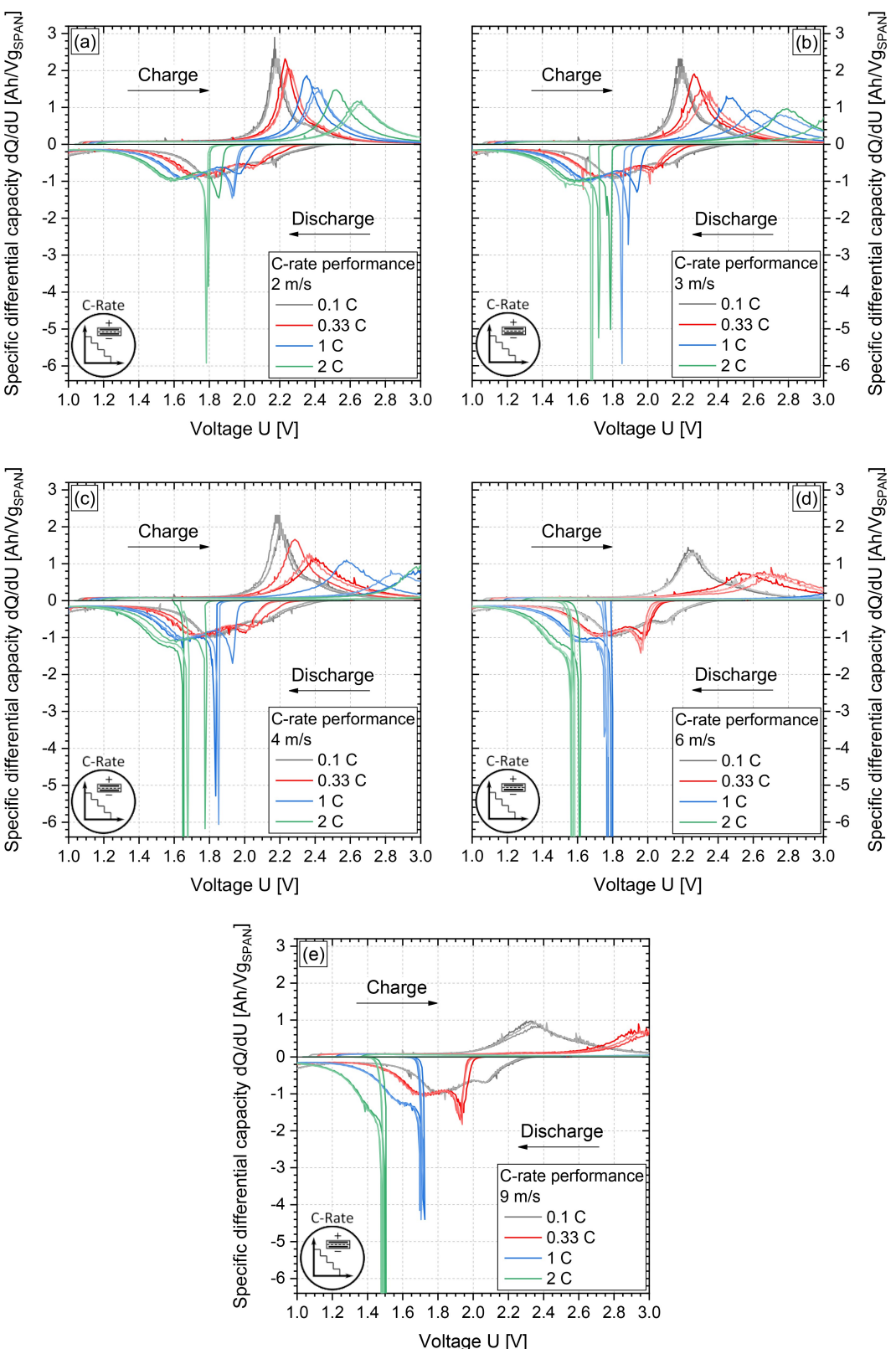


Figure 5. Voltage characteristics are shown as specific differential capacities for the different tip speeds and C-rates, respectively. The middle of the three test cycles is shown for each C-rate and all three to four cells, which were cycled. Discharge and charge characteristics are not derived from the same cycle but from their respective rate tests.

specific surface area, the particle size of the active material during the slurry-mixing step, the residual moisture (since the active material is hygroscopic and should adhere water to all accessible surfaces) or the electrode porosity. However, none of these measurements shows any significant impact of the tip speed on the respective electrode properties. Neither the particle size distribution of the diluted slurries (Figure S2 (b)) nor the specific surface area of the electrodes (Figure S5) nor their pore size distribution (Figure S6) show any significant changes or trends. The residual moisture analysis with KFT resulted in values of 5.21, 5.34, 5.12, 5.22, and 5.06 wt.-% for 2, 3, 4, 6, and 9 m s⁻¹, respectively. No major trend or influence could be found there either. Therefore, mechanical damage to the active material can be ruled out as the reason for the degrading performance with higher tip speeds.

Any variation in the reaction mechanism due to changes in the molecular structure of the SPAN can also be ruled out since changes in the reaction mechanism should be visible as significant changes in the dQ/dU plots for increasing tip speeds, e.g., as new peaks. For SPAN, it is proposed that the sulfur chain in the polymer directly reacts to Li₂S₂ and Li₂S via a one-phase solid-solid reaction without forming longer-chain polysulfides. Larger polysulfides (Li₂S₈, Li₂S₆) should be visible in the discharge voltage range as a peak around 2.3 to 2.4 V for low C-rates.^[3,25,26] This peak in the dQ/dU diagram is not visible for any cell, which aligns with the post-mortem optical inspection of the cell components. No coloring of the separator or other components was visible, as shown in Figure S7, which would usually indicate soluble polysulfide formation. This is further supported by the 0.1 C performance of the different cells during the check-up cycles. Since the formation of polysulfides during cycling would lead to a loss of active sulfur material, the achievable capacity at low C-rates should also be impacted, excluding the superposing influence of capacity loss due to higher C-rates. However, by comparing the capacity of the 5th and the 138th cycle, capacity losses of only 0%, 2.6%, 3.9%, 2.8%, and 3.2% can be observed for 2, 3, 4, 6, and 9 m/s, respectively, as shown in more detail in Figure S8. This is

equivalent to a capacity loss of less than 0.03% per cycle, including also classical aging-related capacity losses. All cells show the characteristic double peak of Li₂S₂ and Li₂S in the voltage range between 1.6 and 2.2 V for 0.1 C without any signs regarding the formation of longer polysulfides within the cells. Furthermore, Raman spectroscopy measurements on dry electrodes before cell assembly, as depicted in Figure S9, show no significant differences. These are strong indications that the capacity loss of the SPAN cells is not based on changes in the reaction mechanism e.g. due to the formation of longer chain polysulfide during cycling.

The third possible reason is the ionic conductivity within the electrode. The ionic conductivity of an electrode in a cell usually depends on the electrolyte's ionic conductivity and the electrode's pore network. Important parameters describing this network are the pore size distribution and the associated tortuosity.^[87,88] As already discussed above, the electrodes have no significant difference in their pore size distribution, as shown in Figure S6. Therefore, a substantial difference in the tortuosity of the electrodes is very unlikely, suggesting that the pore network of the electrode itself is not the reason for the electrochemical performance differences.

The last possible factor is the electrical connection within the electrode. A higher tip speed means higher shear stress during mixing, which leads to an increased deagglomeration of carbon black and, therefore, smaller carbon black particles, which has extensively been shown for LIBs in the past.^[86,89,90] This is also true for the herein-produced SPAN-electrodes, as shown in Figure 6(a) for slurry samples where the active material was centrifuged beforehand. The amount of carbon black aggregates increases with rising tip speed while the amount of agglomerates decreases and the agglomerates get smaller. This change in the carbon black particle size distribution can be easily described by the dispersion index (DI) defined by Weber et al.^[91] A higher DI correlates with a larger fraction of smaller carbon black aggregates, or in other words, a higher degree of deagglomeration. When looking into the dependence of the electrodes' resistivity (measured by two different

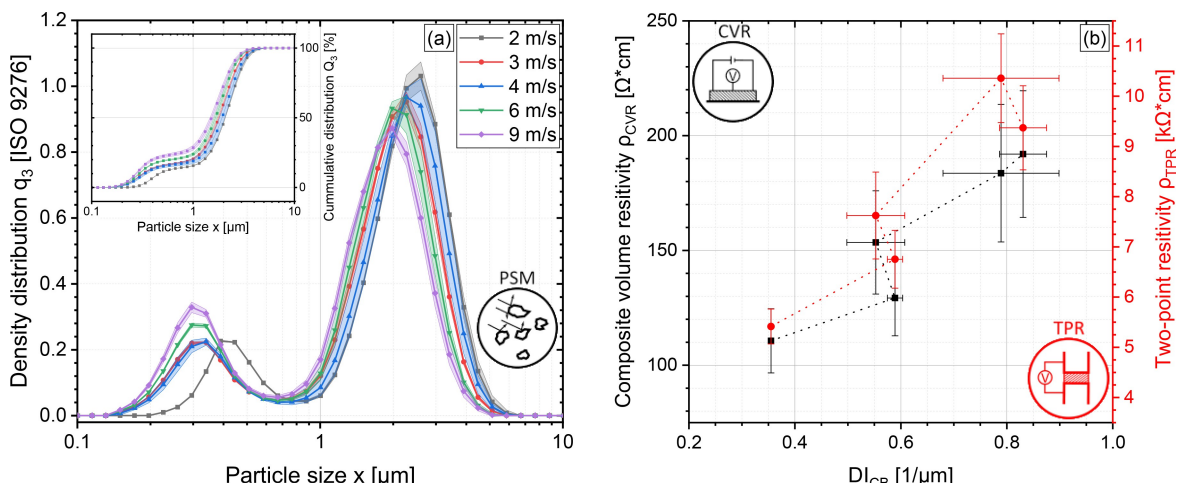


Figure 6. Particle size distribution of centrifuged slurry samples at the end of the third mixing step (AM addition) (a) and electrode resistivity measured by multipoint and two-point approach in dependence of the carbon black dispersion index (DI) by Weber et al.^[91] (b).

techniques) on the DI, it can be seen that for higher DIs the resistivity increases. This shows that the electrical percolation in the electrode is getting worse because smaller carbon black particles are less capable of bridging longer distances.^[85,92] Since the SPAN active material has a comparably low intrinsic electrical conductivity of about $10^{-3} \text{ mS cm}^{-1}$ to $10^{-1} \text{ mS cm}^{-1}$,^[34,76] more or less comparable to classical LIB cathode active materials like NCM or LFP, the carbon black has to form a percolation network within the whole electrode for good electrical connection.^[34] This network is getting worse for higher tip speeds, as shown in Figure 6(b).

However, a pure electrical influence would be expected to be symmetric, but since SPAN is a conversion material, the formation and dissolution of Li_2S_2 and Li_2S reaction products could be an aspect. The reaction of sulfur is generally much more sluggish and kinetically limited during oxidation due to the kinetic limitations associated with the conversion of the Li_2S_2 and Li_2S solid crystallites in the electrode.^[93–96] Additionally, Li_2S_2 and Li_2S show a significantly lower electrical conductivity compared to SPAN of 3.6×10^{-4} to $1 \times 10^{-11} \text{ mS cm}^{-1}$, depending on the source.^[11,97–99] In combination with the diminishing percolation of carbon black in the electrode at higher tip speeds, this could amplify the already prominent kinetic limitations in the oxidation step, leading to increased overpotentials during charging. This assumption aligns with the fact that the C-rate performance in charge direction is already worse for 2 ms^{-1} compared to the discharge performance despite the internal resistance in charge and discharge direction being very similar. Another contributing factor might be the volume expansion of SPAN during reduction of approximately 50%.^[27] This might lead to a loss of CB percolation in the expanded electrodes, especially if the electrical connection in the electrodes produced with higher tip speeds is already worse.

Summarizing the results: the most probable influence leading to the worsening charge performance of the electrodes with higher tip speeds is an increase in the electrical charge transfer resistance during the Li_2S_2 and Li_2S oxidation reactions. Since deep mechanistic investigations were not in the scope of this paper, the exact mechanism leading to this effect is still up for debate. However, regarding the mechanical process limit of the SPAN material, our findings indicate no definitive limit where shear stress starts to show a negative impact. An increased shear stress always seems to have a negative effect on the electrodes' overpotentials, especially for the charge direction. This leads to lower C-rate performance, lower energy efficiency due to an enlarged voltage difference between charge and discharge, and faster capacity fading.

The energy density and the gravimetric energy are essential parameters for any battery application. Therefore, we would like to shed some light on this aspect for SPAN-based electrodes. Besides all its benefits described here and in other papers, a major drawback of the SPAN material is the amount of inactive backbone weight, lowering its specific capacity, energy density, and specific energy. This is shown by the low energy values of 267.2 Wh L^{-1} and 123.7 Wh kg^{-1} in Table S3 for a non-optimized baseline electrode, which is an almost direct extrapolation of our coin cell setup to a larger cell stack.

Therefore, a critical factor for improving the cell's energy values in the future is an increase of the active material capacity by increasing the gravimetric amount of sulfur within the polymer. This can be done by:

- 1) Introducing longer sulfur chains, which leads to a higher risk of polysulfide formation.
- 2) Introducing a higher density of sulfur chains, which is limited by appropriate connection sites.
- 3) Reducing the weight of the backbone.

Different backbones show the possibility of increasing the sulfur content in SPAN-equivalent materials to up to 68 wt-%,^[22] which would correlate with a theoretical specific capacity of the material of about 1135 mAh g^{-1} , but have their own drawbacks.

As shown by our calculation in Table S3, further improvement of the energy density or specific energy of SPAN cells can be achieved by optimizing the cathode as a whole through:

- 1) Increasing the electrode's density by calendering to reduce the necessary electrolyte amount.
- 2) Increasing the areal loading of the electrodes.
- 3) Increasing the SPAN content within the cathode.

Reducing the necessary electrolyte amount is one of the most important factors to improve the energy values of Lithium-sulfur cells, as also stated by Dörfler et al., Betz et al., or Yang et al.^[7,11,100] However, reducing the electrolyte amount and the cathode porosity or increasing the areal loading can lead to slower kinetics, worse cycling stability, or faster cell failure if not optimized correctly. It becomes evident that improving the cell performance and energy values is an interconnected problem with a multitude of components and influence factors even with SPAN as the active material and, therefore, no easy task. However, highly optimized cells with high-sulfur SPAN-equivalent materials can achieve supreme energy values of more than 700 Wh L^{-1} and 500 Wh kg^{-1} on stack level, as calculated in Table S3. These values are competitive not only with classical LIBs but also with values proposed for optimized lithium-sulfur cells using elemental sulfur.^[11,100] That's why a combination of material and processing research has to be pursued in the future to achieve industrial competitiveness and usability of the auspicious SPAN material.

Conclusion and Outlook

Sulfur polyacrylonitrile (SPAN) is a very promising cathode active material for lithium-sulfur batteries with high cycling stability and good performance. In this study, the processing behavior of an industrially scalable SPAN material under various slurry mixing conditions using different tip speeds was investigated. The intermediary products as well as the final electrodes were thoroughly analyzed. All SPAN slurries showed good processability during slurry mixing, coating, and drying due to their highly viscous and gel-like behavior at low shear rates and a free-flowing and low viscosity behavior at high shear rates. Coin cells were built from the uncalendered electrodes and investigated electrochemically. These tests revealed that higher shear stresses introduced by higher mixing tip speeds lead to

increased internal resistances of the cells, especially in charge direction, resulting in increased overpotentials. This asymmetric increase in internal resistance posed some questions about the origin of this behavior. Based on the characterization of the electrodes by BET, particle size, pore size, residual moisture and Raman measurements, a mechanical fracture/stressing of the active material, a change in the reaction mechanism and a worsening electrode tortuosity were ruled out. Instead, the evidence points towards an increased electrical resistivity of the electrode due to decreasing carbon black percolation at higher tip speeds in combination with the kinetic limitation of sulfur cathodes during Li_2S_2 and Li_2S oxidation. However, clarification of the exact mechanism leading to this asymmetric capacity decay requires additional investigation. Nevertheless, one clear conclusion emerges: increased shear stress during wet mixing leads to worse electrochemical performance. Therefore, the SPAN slurry should be mixed gently. Since a deagglomeration of carbon black in case of higher mixing intensities leads to higher electrical resistivity and the slurry has an excellent processing behavior, slow mixing speeds and short mixing times do not have to be drawbacks. They can reduce the energy demand during production and lower the factory footprint since the number of mixing devices can be lower. The performance of SPAN could also be further improved in the future by enhancing its kinetics through optimization of the particle morphology as well as the pore structure, by increasing the electrical conductivity of the electrode with advanced conductive agents or catalytic additives, or by raising the sulfur content and optimization of the polymer backbone.

Conclusively, it was shown that SPAN material, when processed under the correct conditions, offers a very stable cycling behavior in ether-based electrolytes without noticeable polysulfide formation. However, the cells energy values, rate- and long-term cycling performance depend on many parameters such as processing, areal loading, cathode porosity, lithium-anode dendrite formation characteristics and SEI formation, electrolyte amount and type, as well as the separator properties. The production and research of lithium-sulfur batteries remain challenging, even with SPAN as an active material suppressing the shuttle effect. Nevertheless, we think the material is promising in its properties and processability and thus ready to jump from lab-scale material research to scalable and industry-relevant processing research.

Acknowledgements

The authors thank Jakub Stasiak, Alexander Neuberger, and Markus Schubert for assisting with the experimental work, as well as the German Federal Ministry for Economic Affairs and Climate Action and the German Federal Ministry of Education and Research for the funding in the wake of the projects EVOLi²S [03ETE009G] and SulForFlight [03XP0491B]. Additional thanks go to Toru Yano and ADEKA CORPORATION for assistance in setting up the initial electrode production process, delivery of the SPAN material, and the scientific discussion. Open Access funding enabled and organized by Projekt DEAL.

Conflict of Interests

The authors declare no conflict of interest.

Data Availability Statement

The data that support the findings of this study are available from the corresponding author upon reasonable request.

Keywords: Lithium-Sulfur battery · SPAN · Slurry mixing · Electrode production · Differential capacity

- [1] N. Nitta, F. Wu, J. T. Lee, G. Yushin, *Mater. Today* **2015**, *18*, 252–264. <https://doi.org/10.1016/j.mattod.2014.10.040>.
- [2] B. E. Murdock, K. E. Toghill, N. Tapia-Ruiz, *Adv. Energy Mater.* **2021**, *11*, 2102028. <https://doi.org/10.1002/aenm.202102028>.
- [3] A. Eftekhari, D.-W. Kim, *J. Mater. Chem. A* **2017**, *5*, 17734–17776. <https://doi.org/10.1039/c7ta00799j>.
- [4] J. Li, J. Fleetwood, W. B. Hawley, W. Kays, *Chem. Rev.* **2022**, *155*, 903–956. <https://doi.org/10.1021/acs.chemrev.1c00565>.
- [5] M. Akhilash, P. S. Salini, B. John, T. D. Mercy, *J. Alloys Compd.* **2021**, *869*, 159239. <https://doi.org/10.1016/j.jallcom.2021.159239>.
- [6] M. Kotal, S. Jakhari, S. Roy, H. K. Sharma, *J. Energy Storage* **2022**, *47*, 103534. <https://doi.org/10.1016/j.est.2021.103534>.
- [7] S. Dörfler, H. Althues, P. Härtel, T. Abendroth, B. Schumm, S. Kaskel, *Joule* **2020**, *4*, 539–554. <https://doi.org/10.1016/j.joule.2020.02.006>.
- [8] E. Peled, I. Shekhtman, T. Mukra, M. Goor, I. Belenkaya, D. Golodnitsky, *J. Electrochem. Soc.* **2018**, *165*, A6051–A6057. <https://doi.org/10.1149/2.0101801jes>.
- [9] B. Wang, S. M. Alhassan, S. T. Pantelides, *Phys. Rev. Appl.* **2014**, *2*, <https://doi.org/10.1103/PhysRevApplied.2.034004>.
- [10] R. Fang, S. Zhao, Z. Sun, D.-W. Wang, H.-M. Cheng, F. Li, *Adv. Mater.* **2017**, *29*. <https://doi.org/10.1002/adma.201606823>.
- [11] X. Yang, X. Li, K. Adair, H. Zhang, X. Sun, *Electrochem. Energy Rev.* **2018**, *1*, 239–293. <https://doi.org/10.1007/s41918-018-0010-3>.
- [12] Y. Chen, T. Wang, H. Tian, D. Su, Q. Zhang, G. Wang, *Adv. Mater.* **2021**, *33*, e2003666. <https://doi.org/10.1002/adma.202003666>.
- [13] S. S. Zhang, *J. Power Sources* **2007**, *164*, 351–364. <https://doi.org/10.1016/j.jpowsour.2006.10.065>.
- [14] S. Li, B. Jin, X. Zhai, H. Li, Q. Jiang, *ChemistrySelect* **2018**, *3*, 2245–2260. <https://doi.org/10.1002/slct.201703112>.
- [15] Y.-T. Weng, H. Wang, R.-C. Lee, C.-Y. Huang, S.-S. Huang, M. Abdollahifar, L.-M. Kuo, B.-J. Hwang, C.-L. Kuo, Y. Cui, N.-L. Wu, *J. Power Sources* **2020**, *450*, 227676. <https://doi.org/10.1016/j.jpowsour.2019.227676>.
- [16] T. Liu, H. Hu, X. Ding, H. Yuan, C. Jin, J. Nai, Y. Liu, Y. Wang, Y. Wan, X. Tao, *Energy Storage Mater.* **2020**, *30*, 346–366. <https://doi.org/10.1016/j.ensm.2020.05.023>.
- [17] H. Wang, W. Zhang, J. Xu, Z. Guo, *Adv. Funct. Mater.* **2018**, *28*, 1707520. <https://doi.org/10.1002/adfm.201707520>.
- [18] H. Ye, J. Y. Lee, *Small Methods* **2020**, *4*, 1900864. <https://doi.org/10.1002/smtd.201900864>.
- [19] S. S. Zhang, *Front. Energy Res.* **2013**, *1*, <https://doi.org/10.3389/fenrg.2013.00010>.
- [20] Y. Liu, Y. Elias, J. Meng, D. Aurbach, R. Zou, D. Xia, Q. Pang, *Joule* **2021**, *5*, 2323–2364. <https://doi.org/10.1016/j.joule.2021.06.009>.
- [21] Z. Pan, D. J. L. Brett, G. He, I. P. Parkin, *Adv. Energy Mater.* **2022**, *12*, 2103483. <https://doi.org/10.1002/aenm.202103483>.
- [22] Q. Du, M. Benedek, K. Küster, T. Acartürk, U. Starke, J.-L. Hoslauer, T. Schleid, M. R. Buchmeiser, *Batteries & Supercaps* **2022**, *5*, <https://doi.org/10.1002/batt.202200277>.
- [23] L. Wang, X. He, J. Li, M. Chen, J. Gao, C. Jiang, *Electrochim. Acta* **2012**, *72*, 114–119. <https://doi.org/10.1016/j.electacta.2012.04.005>.
- [24] X. Wang, Y. Qian, L. Wang, H. Yang, H. Li, Y. Zhao, T. Liu, *Adv. Funct. Mater.* **2019**, *29*, 1902929. <https://doi.org/10.1002/adfm.201902929>.
- [25] S. Warneke, M. Eusterholz, R. K. Zenn, A. Hintennach, R. E. Dinnebier, M. R. Buchmeiser, *J. Electrochem. Soc.* **2018**, *165*, A6017–A6020. <https://doi.org/10.1149/2.0061801jes>.

- [26] S. Wei, L. Ma, K. E. Hendrickson, Z. Tu, L. A. Archer, *J. Am. Chem. Soc.* **2015**, *137*, 12143–12152. <https://doi.org/10.1021/jacs.5b08113>.
- [27] S. Perez Beltran, P. B. Balbuena, *J. Phys. Chem. C* **2021**, *125*, 13185–13194. <https://doi.org/10.1021/acs.jpcc.1c02966>.
- [28] M. S. Ahmed, S. Lee, M. Agostini, M.-G. Jeong, H.-G. Jung, J. Ming, Y.-K. Sun, J. Kim, J.-Y. Hwang, *Adv. Sci.* **2021**, *8*, e2101123. <https://doi.org/10.1002/advs.202101123>.
- [29] J. Wang, J. Yang, J. Xie, N. Xu, *Adv. Mater.* **2002**, *14*, 963–965. [https://doi.org/10.1002/1521-4095\(20020705\)14:13/14<963:AID-ADMA963>3.0.CO;2-P](https://doi.org/10.1002/1521-4095(20020705)14:13/14<963:AID-ADMA963>3.0.CO;2-P).
- [30] X. Zhao, C. Wang, Z. Li, X. Hu, A. Abdul Razzaq, Z. Deng, *J. Mater. Chem. A* **2021**, *9*, 19282–19297. <https://doi.org/10.1039/DITA03300J>.
- [31] L. Wang, X. He, J. Li, J. Gao, J. Guo, C. Jiang, C. Wan, *J. Mater. Chem.* **2012**, *22*, 22077. <https://doi.org/10.1039/c2jm30632h>.
- [32] J. Fanous, M. Wegner, M. B. M. Spera, M. R. Buchmeiser, *J. Electrochem. Soc.* **2013**, *160*, A1169–A1170. <https://doi.org/10.1149/2.052308jes>.
- [33] L. Wang, J. Zhao, X. He, C. Wan, *Electrochim. Acta* **2011**, *56*, 5252–5256. <https://doi.org/10.1016/j.electacta.2011.03.009>.
- [34] L. Yin, J. Wang, F. Lin, J. Yang, Y. Nuli, *Energy Environ. Sci.* **2012**, *5*, 6966. <https://doi.org/10.1039/c2ee03495f>.
- [35] L. Yin, J. Wang, J. Yang, Y. Nuli, *J. Mater. Chem.* **2011**, *21*, 6807. <https://doi.org/10.1039/c1jm00047k>.
- [36] Q. Wu, W. Zhang, S. Li, W. Zhong, H. Zhu, Z. Zeng, C. Yu, S. Cheng, J. Xie, *ACS Appl. Energ. Mater.* **2022**, *5*, 5212–5218. <https://doi.org/10.1021/acsaem.2c00585>.
- [37] J. Li, K. Li, M. Li, D. Gosselink, Y. Zhang, P. Chen, *J. Power Sources* **2014**, *252*, 107–112. <https://doi.org/10.1016/j.jpowsour.2013.11.088>.
- [38] J. Wang, L. Yin, H. Jia, H. Yu, Y. He, J. Yang, C. W. Monroe, *ChemSusChem* **2014**, *7*, 563–569. <https://doi.org/10.1002/cssc.201300742>.
- [39] T. Wang, Q. Zhang, J. Zhong, M. Chen, H. Deng, J. Cao, L. Wang, L. Peng, J. Zhu, B. Lu, *Adv. Energy Mater.* **2021**, *11*. <https://doi.org/10.1002/aenm.202100448>.
- [40] Q. Wu, M. Qin, Y. Wu, H. Zhu, S. Cheng, J. Xie, *J. Mater. Chem. A* **2023**, *11*, 22913–22921. <https://doi.org/10.1039/D3TA04860H>.
- [41] Z. Han, S. Li, R. Xiong, Z. Jiang, M. Sun, W. Hu, L. Peng, R. He, H. Zhou, C. Yu, S. Cheng, J. Xie, *Adv. Funct. Mater.* **2022**, *32*. <https://doi.org/10.1002/adfm.202108669>.
- [42] J. Xiang, Z. Guo, Z. Yi, Y. Zhang, L. Yuan, Z. Cheng, Y. Shen, Y. Huang, *J. Energy Chem.* **2020**, *49*, 161–165. <https://doi.org/10.1016/j.jecchem.2020.01.037>.
- [43] Y. Li, S. Zhang, H. Liu, Y. Zhang, X. Zhang, *ACS Appl. Energ. Mater.* **2023**, *6*, 8511–8520. <https://doi.org/10.1021/acsaem.3c01366>.
- [44] M. Frey, R. K. Zenn, S. Warneke, K. Müller, A. Hintennach, R. E. Dinnebier, M. R. Buchmeiser, *ACS Energy Lett.* **2017**, *2*, 595–604. <https://doi.org/10.1021/acsenergylett.7b00009>.
- [45] Y. Liu, A. K. Haridas, Y. Lee, K.-K. Cho, J.-H. Ahn, *Appl. Surf. Sci.* **2019**, *472*, 135–142. <https://doi.org/10.1016/j.apsusc.2018.03.062>.
- [46] S. Kalybekkyzy, A. Mentbayeva, M. V. Kahraman, Y. Zhang, Z. Bakenov, *J. Electrochem. Soc.* **2019**, *166*, A5396–A5402. <https://doi.org/10.1149/2.0571903jes>.
- [47] K. Wang, T. Zhao, N. Zhang, T. Feng, L. Li, F. Wu, R. Chen, *Nanoscale* **2021**, *13*, 16690–16695. <https://doi.org/10.1039/d1nr04825b>.
- [48] Y. Liu, A. K. Haridas, K.-K. Cho, Y. Lee, J.-H. Ahn, *J. Phys. Chem. C* **2017**, *121*, 26172–26179. <https://doi.org/10.1021/acs.jpcc.7b06625>.
- [49] J. Lei, J. Chen, A. Naveed, H. Zhang, J. Yang, Y. Nuli, J. Wang, *ACS Appl. Energ. Mater.* **2021**, *4*, 5706–5712. <https://doi.org/10.1021/acsaem.1c00556>.
- [50] Y. Zhang, Y. Zhao, Z. Bakenov, A. Konarov, P. Chen, *J. Power Sources* **2014**, *270*, 326–331. <https://doi.org/10.1016/j.jpowsour.2014.07.096>.
- [51] X. Chen, L. Peng, L. Wang, J. Yang, Z. Hao, J. Xiang, K. Yuan, Y. Huang, B. Shan, L. Yuan, J. Xie, *Nat. Commun.* **2019**, *10*, 1021. <https://doi.org/10.1038/s41467-019-08818-6>.
- [52] Y. Zhang, Y. Sun, L. Peng, J. Yang, H. Jia, Z. Zhang, B. Shan, J. Xie, *Energy Storage Mater.* **2019**, *21*, 287–296. <https://doi.org/10.1016/j.ensm.2018.12.010>.
- [53] R. He, Y. Li, Z. Yin, H. Liu, Y. Jin, Y. Zhang, H. Liu, X. Zhang, *ACS Appl. Energ. Mater.* **2023**, *6*, 3903–3914. <https://doi.org/10.1021/acsaem.3c00067>.
- [54] R. He, Y. Li, S. Wei, H. Liu, S. Zhang, N. Han, H. Liu, X. Wang, X. Zhang, *J. Alloys Compd.* **2022**, *919*, 165838. <https://doi.org/10.1016/j.jallcom.2022.165838>.
- [55] S. Li, Z. Han, W. Hu, L. Peng, J. Yang, L. Wang, Y. Zhang, B. Shan, J. Xie, *Nano Energy* **2019**, *60*, 153–161. <https://doi.org/10.1016/j.nanoen.2019.03.023>.
- [56] S. Ma, Z. Zhang, Y. Wang, Z. Yu, C. Cui, M. He, H. Huo, G. Yin, P. Zuo, *Chem. Eng. J.* **2021**, *418*, 129410. <https://doi.org/10.1016/j.cej.2021.129410>.
- [57] W. B. Hawley, J. Li, *J. Energy Storage* **2019**, *25*, 100862. <https://doi.org/10.1016/j.est.2019.100862>.
- [58] V. Wenzel, H. Nirschl, D. Nötzel, *Energy Technol.* **2015**, *3*, 692–698. <https://doi.org/10.1002/ente.201402218>.
- [59] L.-C. Chen, D. Liu, T.-J. Liu, C. Tiu, C.-R. Yang, W.-B. Chu, C.-C. Wan, *J. Energy Storage* **2016**, *5*, 156–162. <https://doi.org/10.1016/j.est.2015.12.008>.
- [60] S. Jaiser, A. Friske, M. Baunach, P. Scharfer, W. Schabel, *Drying Technol.* **2017**, *35*, 1266–1275. <https://doi.org/10.1080/07373937.2016.1248975>.
- [61] B. Westphal, H. Bockholt, T. Gunther, W. Haselrieder, A. Kwade, *ECS Trans.* **2015**, *64*, 57–68. <https://doi.org/10.1149/06422.0057ecst>.
- [62] M. Abdollahifar, H. Cavers, S. Scheffler, A. Diener, M. Lippke, A. Kwade, *Adv. Energy Mater.* **2023**, *13*, 2300973. <https://doi.org/10.1002/aenm.202300973>.
- [63] A. Kwade, W. Haselrieder, R. Leithoff, A. Modlinger, F. Dietrich, K. Droeder, *Nat. Energy* **2018**, *3*, 290–300. <https://doi.org/10.1038/s41560-018-0130-3>.
- [64] P. Li, X. Xia, J. Guo, *Sep. Purif. Technol.* **2022**, *296*, 121389. <https://doi.org/10.1016/j.seppur.2022.121389>.
- [65] H. Dreger, M. Huelsebrock, L. Froboese, A. Kwade, *Ind. Eng. Chem. Res.* **2017**, *56*, 2466–2474. <https://doi.org/10.1021/acs.iecr.6b02103>.
- [66] L. Froboese, P. Titscher, B. Westphal, W. Haselrieder, A. Kwade, *Mater. Charact.* **2017**, *133*, 102–111. <https://doi.org/10.1016/j.matchar.2017.09.002>.
- [67] B. G. Westphal, N. Mainusch, C. Meyer, W. Haselrieder, M. Indrikova, P. Titscher, H. Bockholt, W. Viöl, A. Kwade, *J. Energy Storage* **2017**, *11*, 76–85. <https://doi.org/10.1016/j.est.2017.02.001>.
- [68] F. Huttner, W. Haselrieder, A. Kwade, *Energy Technol.* **2020**, *8*, 1900245. <https://doi.org/10.1002/ente.201900245>.
- [69] K. Ryll, L. Hoffmann, O. Landrath, F. Lienesch, M. Kurat, *Batteries* **2021**, *7*, 9. <https://doi.org/10.3390/batteries7010009>.
- [70] M. Haarmann, W. Haselrieder, A. Kwade, *Energy Technol.* **2020**, *8*, 1801169. <https://doi.org/10.1002/ente.201801169>.
- [71] M. Weber, R. Moschner, A. Kwade, *Energy Technol.* **2023**, *11*. <https://doi.org/10.1002/ente.202200852>.
- [72] T. Mezger, *The rheology handbook: For users of rotational and oscillatory rheometers*, 5th revised edition, Vincentz, Hannover, 2020.
- [73] W. B. Hawley, J. Li, *J. Energy Storage* **2019**, *26*, 100994. <https://doi.org/10.1016/j.est.2019.100994>.
- [74] F. Röder, V. Laue, U. Kremer, *Batteries & Supercaps* **2019**, *2*, 248–265. <https://doi.org/10.1002/batt.201800107>.
- [75] S. K. Heiskanen, J. Kim, B. L. Lucht, *Joule* **2019**, *3*, 2322–2333. <https://doi.org/10.1016/j.joule.2019.08.018>.
- [76] R. Mukkabala, M. R. Buchmeiser, *J. Mater. Chem. A* **2020**, *8*, 5379–5394. <https://doi.org/10.1039/c9ta12619h>.
- [77] D. Kashchiev, G. M. van Rosmalen, *Cryst. Res. Technol.* **2003**, *38*, 555–574. <https://doi.org/10.1002/crat.200310070>.
- [78] P. G. Vekilov, *Cryst. Growth Des.* **2010**, *10*, 5007–5019. <https://doi.org/10.1021/cg1011633>.
- [79] L. Bläubaum, F. Röder, C. Nowak, H. S. Chan, A. Kwade, U. Kremer, *ChemElectroChem* **2020**, *7*, 4755–4766. <https://doi.org/10.1002/celc.202001249>.
- [80] A. C. Wagner, N. Bohn, H. Geßwein, M. Neumann, M. Osenberg, A. Hilger, I. Manke, V. Schmidt, J. R. Binder, *ACS Appl. Energ. Mater.* **2020**, *3*, 12565–12574. <https://doi.org/10.1021/acsaem.0c02494>.
- [81] J. Zhang, J. Qiao, K. Sun, Z. Wang, *Particuology* **2022**, *61*, 18–29. <https://doi.org/10.1016/j.partic.2021.05.006>.
- [82] A. Shodiev, M. Chouchane, M. Gaberscek, O. Arcelus, J. Xu, H. Oularbi, J. Yu, J. Li, M. Morcrette, A. A. Franco, *Energy Storage Mater.* **2022**, *47*, 462–471. <https://doi.org/10.1016/j.ensm.2022.01.058>.
- [83] J. Landesfeind, A. Eldiven, H. A. Gasteiger, *J. Electrochem. Soc.* **2018**, *165*, A1122–A1128. <https://doi.org/10.1149/2.0971805jes>.
- [84] S. N. Lauro, J. N. Burrow, C. B. Mullins, *eScience* **2023**, *3*, 100152. <https://doi.org/10.1016/j.esci.2023.100152>.
- [85] H. Bockholt, W. Haselrieder, A. Kwade, *Powder Technol.* **2016**, *297*, 266–274. <https://doi.org/10.1016/j.powtec.2016.04.011>.
- [86] J. Entwistle, R. Ge, K. Pardikar, R. Smith, D. Cumming, *Renewable Sustainable Energy Rev.* **2022**, *166*, 112624. <https://doi.org/10.1016/j.rser.2022.112624>.
- [87] J. Ávila, J. Pagalo, M. Espinoza-Andaluz, *Sci. Rep.* **2022**, *12*, 19463. <https://doi.org/10.1038/s41598-022-23643-6>.

- [88] J. Landesfeind, J. Hattendorff, A. Ehrl, W. A. Wall, H. A. Gasteiger, *J. Electrochem. Soc.* **2016**, *163*, A1373–A1387. <https://doi.org/10.1149/2.1141607jes>.
- [89] D. Grießl, K. Huber, R. Scherbauer, A. Kwade, *Adv. Powder Technol.* **2021**, *32*, 2280–2288. <https://doi.org/10.1016/j.apt.2021.05.003>.
- [90] J. K. Mayer, L. Almar, E. Asylbekov, W. Haselrieder, A. Kwade, A. Weber, H. Nirschl, *Energy Technol.* **2020**, *8*, 1900161. <https://doi.org/10.1002/ente.201900161>.
- [91] M. Weber, J. K. Mayer, A. Kwade, *Energy Technol.* **2023**, *11*, 2201299. <https://doi.org/10.1002/ente.202201299>.
- [92] W. Bauer, D. Nötzel, V. Wenzel, H. Nirschl, *J. Power Sources* **2015**, *288*, 359–367. <https://doi.org/10.1016/j.jpowsour.2015.04.081>.
- [93] H. Cavers, H. Krüger, O. Polonskyi, F. Schütt, R. Adelung, S. Hansen, *ACS Omega* **2020**, *5*, 28196–28203. <https://doi.org/10.1021/acsomega.0c03956>.
- [94] A. Gupta, A. Bhargav, J.-P. Jones, R. V. Bugga, A. Manthiram, *Chem. Mater.* **2020**, *32*, 2070–2077. <https://doi.org/10.1021/acs.chemmater.9b05164>.
- [95] J. Wu, T. Ye, Y. Wang, P. Yang, Q. Wang, W. Kuang, X. Chen, G. Duan, L. Yu, Z. Jin, J. Qin, Y. Lei, *ACS Nano* **2022**, *16*, 15734–15759. <https://doi.org/10.1021/acsnano.2c08581>.
- [96] R. Wang, C. Luo, T. Wang, G. Zhou, Y. Deng, Y. He, Q. Zhang, F. Kang, W. Lv, Q.-H. Yang, *Adv. Mater.* **2020**, *32*, e2000315. <https://doi.org/10.1002/adma.202000315>.
- [97] H. Ye, M. Li, T. Liu, Y. Li, J. Lu, *ACS Energy Lett.* **2020**, *5*, 2234–2245. <https://doi.org/10.1021/acsenergylett.0c00936>.
- [98] S.-H. Chung, C.-H. Chang, A. Manthiram, *Adv. Funct. Mater.* **2018**, *28*. <https://doi.org/10.1002/adfm.201801188>.
- [99] S. Choi, I. Yoon, W. T. Nichols, D. Shin, *Ceram. Int.* **2018**, *44*, 7450–7453. <https://doi.org/10.1016/j.ceramint.2018.01.104>.
- [100] J. Betz, G. Bieker, P. Meister, T. Placke, M. Winter, R. Schmuck, *Adv. Energy Mater.* **2019**, *9*. <https://doi.org/10.1002/aenm.201803170>.

Manuscript received: March 5, 2024

Revised manuscript received: June 18, 2024

Accepted manuscript online: June 21, 2024

Version of record online: August 12, 2024